Oxygen-tailoring in SiO_X/C with a covalent interface for high-performance lithium storage

Jiawei Ge[a], Honglie Shen[a,b*], Fei Zhou[c], Yufang Li[a], Ningyi Yuan[b], Wangyang Yang[a], Haobing Zhou[c] , Binbin Xu[a], Renping Guo [c], Peng Xu[b]

[a]College of Materials Science and Technology, Jiangsu Key Laboratory of Materials and Technology for Energy Conversion, Nanjing University of Aeronautics and Astronautics, Nanjing, 210016, PR China

[b]Jiangsu Collaborative Innovation Center of Photovoltaic Science and Engineering, Changzhou University, Changzhou 213164, P.R. China

[c]College of Mechanical & Electrical Engineering, Nanjing University of Aeronautics and Astronautics, Nanjing, 210016, PR China

[*]Corresponding author: hlshen@nuaa.edu.cn

Tel/Fax: +86-25-52112626

Address: 29 Jiangjun Ave., 211100, Nanjing, China

S1 Material preparation

Porous SiO_2 was prepared through a sol-gel method in our previous work. Typically, CTAB (hexadecyl trimethyl ammonium bromide, 6.2g, Aladdin, AR) was dissolved in distilled water (250ml) and stirred for 1h. And then, TEOS (tetraethyl orthosilicate, 9.2ml, Aladdin, CP) was gently added for a clear solution under stirring. $NH_3 \cdot H_2O$ (ammonium hydroxide, 5ml, Aladdin, CP) was dropped into the solution above to form a SiO_2 gel. After the SiO_2 gel was dried at 90 °C for 24h, porous SiO_2 was prepared through the calcination of dried SiO_2 gel at 550 °C for 5h in air.

Porous SiO_X was prepared through a one-step magnesiothermic reduction reaction (MRR). Typically, porous SiO_2, Mg powder (magnesium, 200 mesh, Sinopharm, ＞99.9%) and KI (potassium iodide, Aladdin, AR) with different mass ratios (1:1.6:2, 1:1:2 and 1:0.6:2, respectively) were uniformly ground and then heated in Ar atmosphere at 650 °C for 6h with a heating rate of 3 °C min^{-1}. The as-prepared powder was immersed in 1 M HCl solution (1M, 100ml, Sinopharm, CP) for 12 h under stirring. Finally, magnesium-reduced SiO_X (denoted as MR-SiO_X) was obtained through centrifugation five times in distilled water and dried at 90 °C for 12h. Following the removal of self-template magnesium oxide (MgO) by hydrochloric acid (HCl) solution, prepared MR-SiO_X is featured with abundant pores and a 3D network. Based on the percentage of magnesium, prepared MR-SiO_X is classified as high MR-SiO_X (HMR-SiO_X), medium MR-SiO_X (MMR-SiO_X) and low MR-SiO_X (LMR-SiO_X).

MR-SiO_X/C was prepared by in-situ polymerization of phenolic resin (denoted as RF) following carbonization. Firstly, MR-SiO_X (0.3g) was put into distilled water

(50ml) for 1h under stirring, and then CTAB (0.1g) and $NH_3 \cdot H_2O$ (1ml) were added into the solution above and stirred for 1h, respectively. Following that, resorcinol (0.2g, Aladdin, AR) and formaldehyde (320μL, Aladdin, AR) were dispersed and stirred for 24h at room temperature. Subsequently, the solution above was transferred into a blast air oven at 85 °C for dried SiO_X@RF. Ultimately, MR-SiO_X/C was obtained through the calcination of SiO_X@RF under Ar atmosphere at 800 °C for 3h with a heating rate of 5 °C min^{-1}.

S2 Material Characterization

X-ray diffraction (XRD, D/max-2500, Rigaku) and X-ray photoelectron spectroscopy (XPS, Thermo Fischer Scientific Multilab 2000 spectrometer) and Raman spectra (LabRAM HR Evolution with 532 nm wavelength incident laser) were performed. The specific surface area along with pore structure was investigated by N_2 adsorption-desorption isotherms (Micromeritics ASAP 2460 analyzer) and measured by Brunauer-Emmett-Teller (BET) method. Thermogravimetric analysis (TGA) was performed on a Netzsch TG 209 apparatus under an air atmosphere with a heating rate of 10 °C min^{-1}. Fourier Transform Infrared Spectrometer (FTIR) was tested on a Thermo-Nicolet iS10 FT-IR spectrometer with 32 scans. The morphological structure of prepared samples was observed in a scanning electron microscope (SEM, SU-8010, HITACHI, Japan). Transmission electron microscope (TEM) and high solution Transmission electron microscope (HRTEM) images were performed on the JEM-2100HR (Tokyo, Japan) to analyze the structure of prepared samples.

S3 Electrochemistry characterization

Followed by drying at 80 °C for 24h in the air, the electrodes were prepared by coating slurries onto copper foil, made up of 80 wt% active material, 10 wt% acetylene black, 10 wt% sodium alginate. And then, the electrodes were punched into circular ones with a diameter of 12 mm. The mass loading of active materials was about 0.8-1.5 mg cm^{-2}. Subsequently, circular electrodes were pressed in 10 MPa for 30 s. Finally, these electrodes were assembled into coin cells (2032 type) in an Ar-filled glove box, which consisted of the electrolyte with 1M $LiPF_6$ in ethylene carbonate and dimethyl carbonate (1:1 vol %) and vinylene carbonate (5 wt %), a counter electrode of lithium metal and a separator of Celgard 2400 film. Galvanostatic curves of these coin cells with voltage from 0.01 to 3 V were tested on the Land automatic batteries tester (LAND-CT2001A, Wuhan, China). Electrochemical impedance spectroscopy (EIS) curves in the frequency range of 1MHz- 1mHz were performed on the electrochemical workstation (CHI660D, Shanghai, China) and Cyclic voltammetry (CV) curves between 0.01 and 3 V at a scan rate of 0.1, 0.3, 0.5, 0.7 and 1 mV s^{-1}.

S4 Simulation and Calculation

Chemomechanical model

Finite element simulation was operated on software ABAQUS/Standard 6.14 for stress distribution. A thermal-mechanical couple model was constructed in place of the Li-diffusion model to analyze stress distribution. The NLgeom was chosen to ensure large geometric changes. The lithium-ion (Li^+) diffusivity (D_{Li+})in the model was simulated in the user-defined subroutines (UMATHT) of the ABAQUS package. Therefore, the normalized Li^+ concentration c, which was changed from 0 (delithiation state) to 1 (full lithiation state), was equivalent to the temperature field. In the initial stage, Li^+ concentrate on the surface was fixed as 1. The thermal expansion coefficient was used to replace the volume expansion coefficient (β) induced by lithium insertion. In our model, the β of Si was set as 0.002, the β of SiO_2 was set as 0.0004, and carbon was kept unchanged based on their volume expansion after full lithiation state. For simplicity and the purpose of exploring stress distribution and evolution upon lithiation, regardless of precisely describing dynamic lithiation behavior, it was assumed that D_{Li+} was a constant. Additionally, it was noted that interfacial separation took place due to the huge differences in material parameters and partitioned grid of Si, SiO_2 and carbon in our model.

Density functional theory (DFT) analysis

The ab-initio simulations were operated in CP2K/Quickstep package within DFT analysis. A hybrid Gaussian and plane-wave formalism with the pseudopotential approximation were used (double-ζ MOLOPT basis sets (DZVP-MOLOPT-SR-GTH) and Goedecker-Teter-Hutter (GTH) pseudopotentials). The cutoff energy of 450 Ry

was set for the plane-wave basis set. All the structures were relaxed until the forces became less than 0.01 eV $Å^{-1}$ with the convergence condition of 1.0×10^{-7}. The ab-initio molecular dynamics (AIMD) analysis was operated to construct amorphous Si and SiO at 2500 K. Among them, a time step of 2 fs and 3000 simulation steps were used. Firstly, cubic Si, containing 16 Si atoms, was constructed with a×b×c of 6.9Å×6.9Å×6.9Å; and cubic SiO containing 16 Si and O atoms was constructed with a×b×c of 8.1Å×8.1Å×8.1Å according to their actual density. Subsequently, the usage of AIMD was to obtain amorphous Si and SiO with a random network model. And then, 16 Li atoms were put into supercell Si and SiO, after which cell optimization of supercell LiSi and LiSiO was carried out. Additionally, to reveal the kinetics properties of Li atoms in Si and SiO, AIMD with a time step of 2 fs and 3000 simulation steps at 1000 K was applied.

Video S1. AIMD simulation of LiSi at 1000K;
Video S2. AIMD simulation of LiSiO at 1000K.

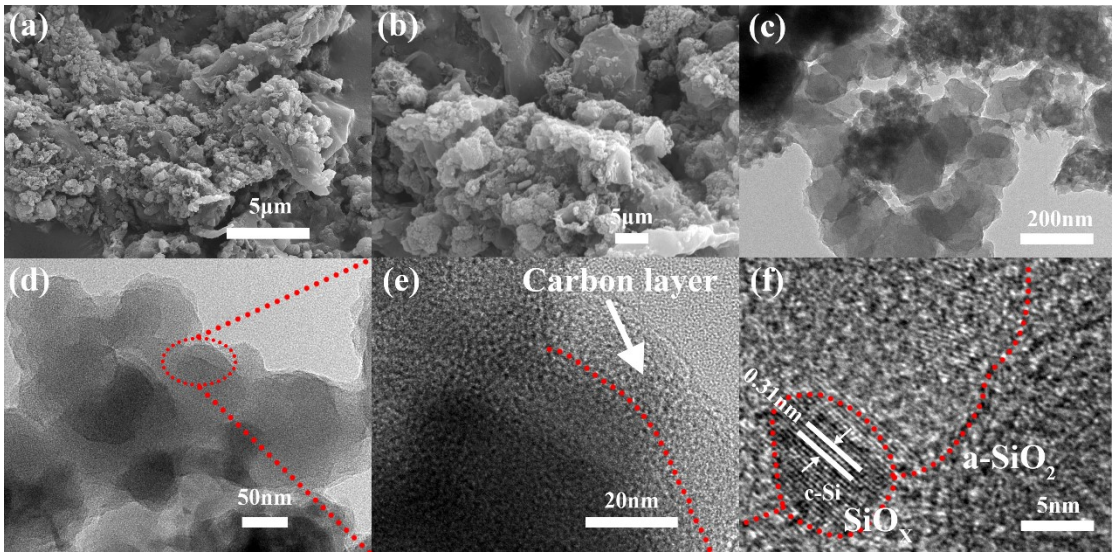

Figure S1 (a-b) SEM images of HMR-SiO_X/C; (c-d) TEM images of HMR-SiO_X/C.

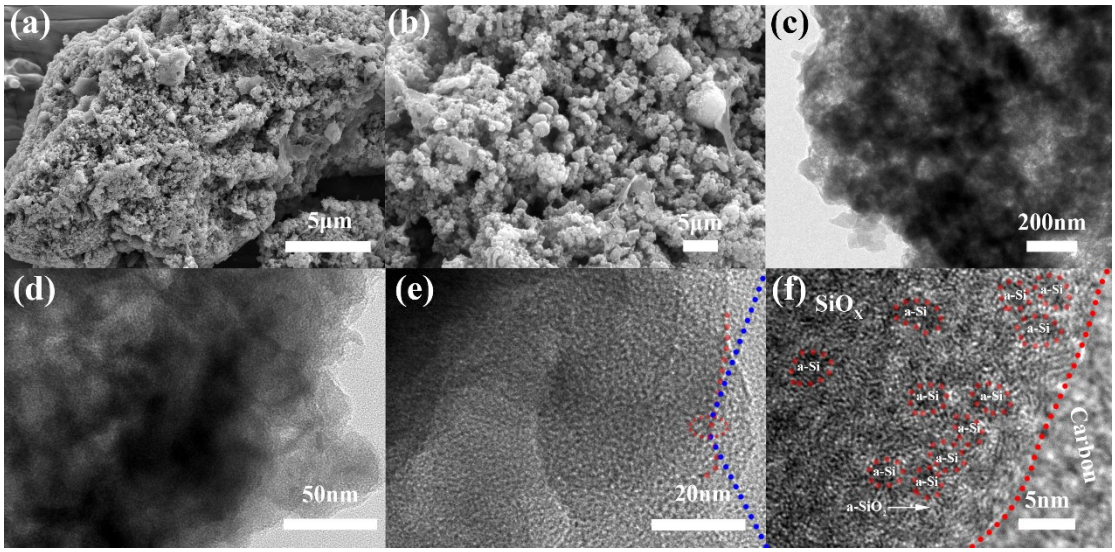

Figure S2 (a-b) SEM images of LMR-SiO$_X$/C; (c-d) TEM images of LMR-SiO$_X$/C

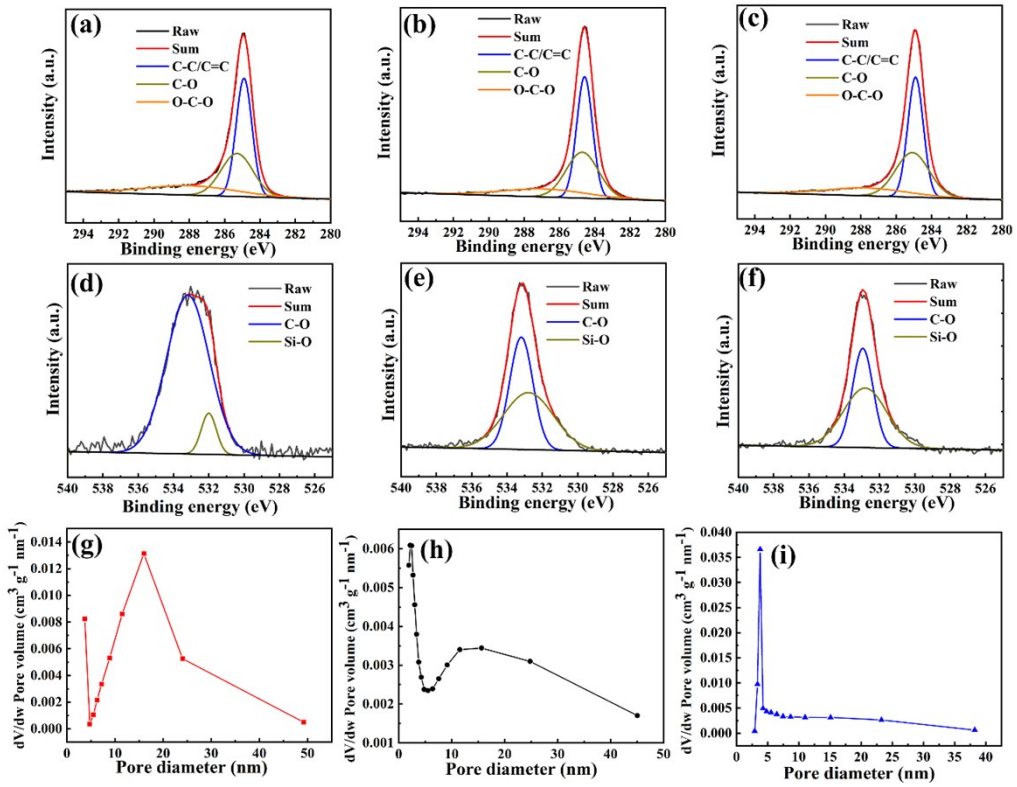

Figure S3 XPS C 1s spectra of (a) HMR-SiO_X/C, (b) MMR-SiO_X/C and (c) LMR-SiO_X/C; XPS O 1s spectra of (d) HMR-SiO_X/C, (e) MMR-SiO_X/C and (f) LMR-SiO_X/C; BJH pore size distribution of (g) HMR-SiO_X/C, (h) MMR-SiO_X/C and (i) LMR-SiO_X/C.

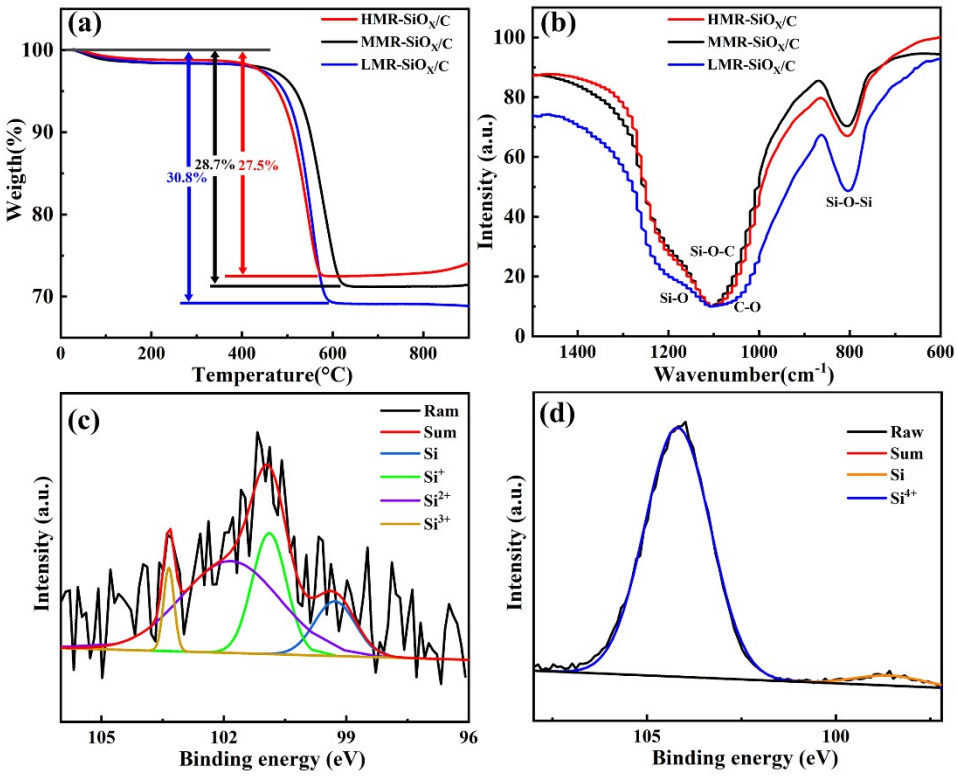

Figure S4 (a) TGA and (b) FTIR spectra; (c) XPS Si 2p spectra of MMR-SiO_X/C-HF; (d) XPS Si 2p spectra of MMR-SiO_X-HF.

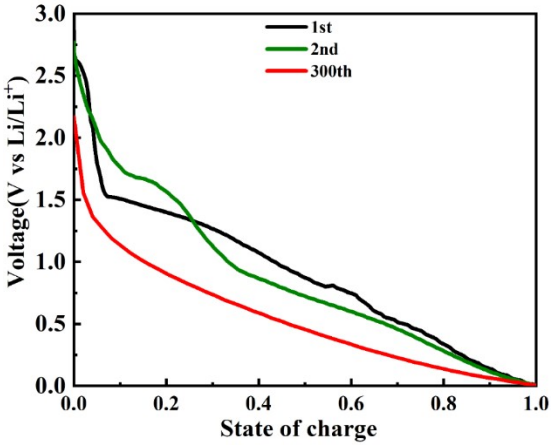

Figure S5 The relationship of state of charge and dynamic voltage for MMR-SiO_X/C

The relationship of state of charge and dynamic voltage can provide a deep understanding of the electrochemical performance of MMR-SiO_X/C. The state of charge is defined based on the specific capacity of MMR-SiO_X/C as shown in Figure S5. The lithiation-delithiaion voltage of MMR-SiO_X/C is higher than that of HMR-SiO_X/C and LMR-SiO_X/C. According to Figure S5, the decomposition of the electrolyte (from ～1.6V) in MMR-SiO_X/C is observed in the initial two cycles, revealing the SEI layer due to the decomposition of the electrolyte continuously grows up on MMR-SiO_X/C for stabilizing its structural integrity. Further, the thickening of the SEI layer suppresses the decomposition of the electrolyte and induces the decrease of the lithiation-delithiation voltage of MMR-SiO_X/C as the relationship of state of charge and dynamic voltage shows after 300 cycles in Figure S5.

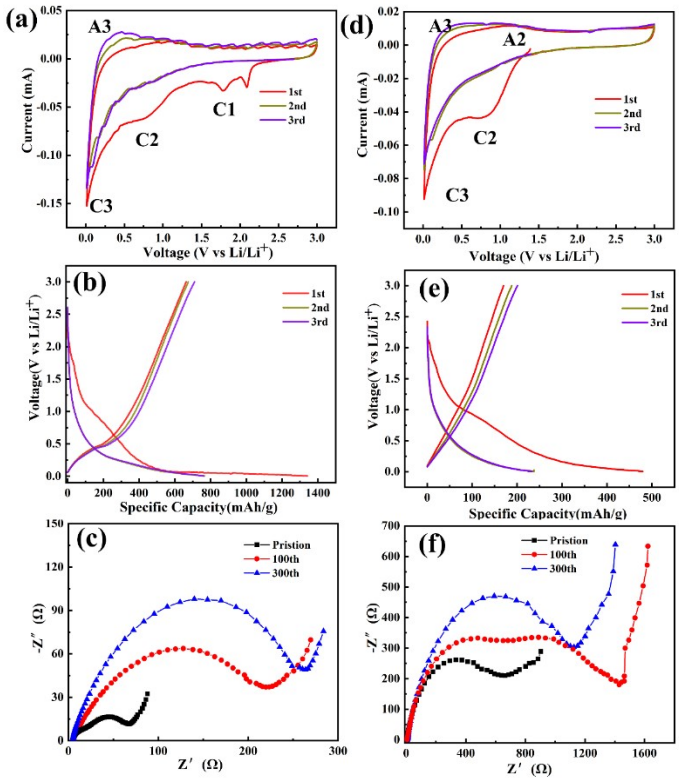

Figure S6 CV curves at a scan rate of 0.1 mV s^{-1} for (a) HMR-SiO_X/C, and (d) LMR-SiO_X/C; Voltage profiles at different cycles at 0.1 A g^{-1} for (b) HMR-SiO_X/C, and (f) LMR-SiO_X/C; EIS spectra of (c) HRR-SiO_X/C and (d) LRR-SiO_X/C.

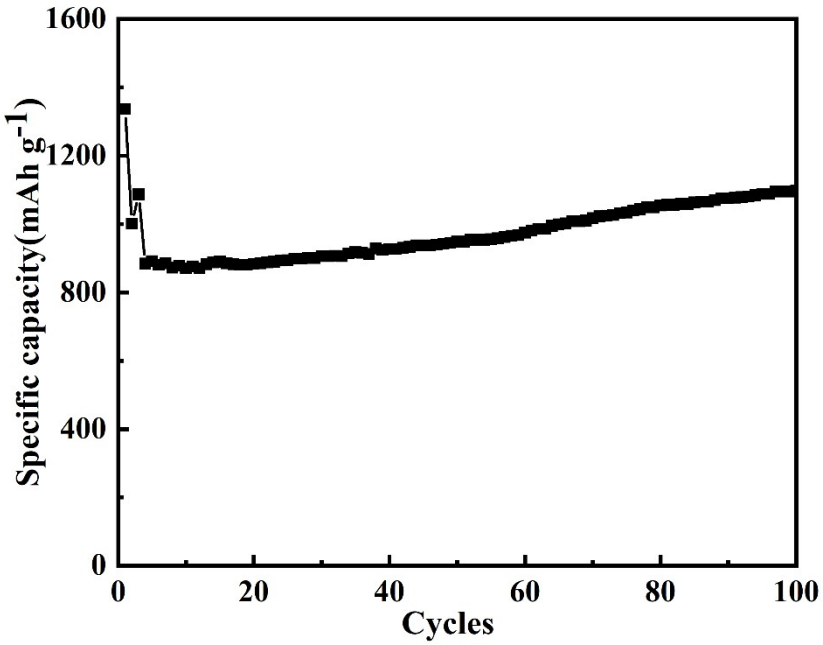

Figure S7 Cycling performance of MMR-SiO_X/C with the voltage window of 1.5-0.01V.

Figure S7 shows the cycling performance of MMR-SiO_X/C with the voltage window of 1.5-0.01 V. The initial discharging capacity of MMR-SiO_X/C is as high as 1337.2 mAh g^{-1}. Its specific capacity still remains 1097.3 mAh g^{-1} with a capacity retention of 82% after 100 cycles.

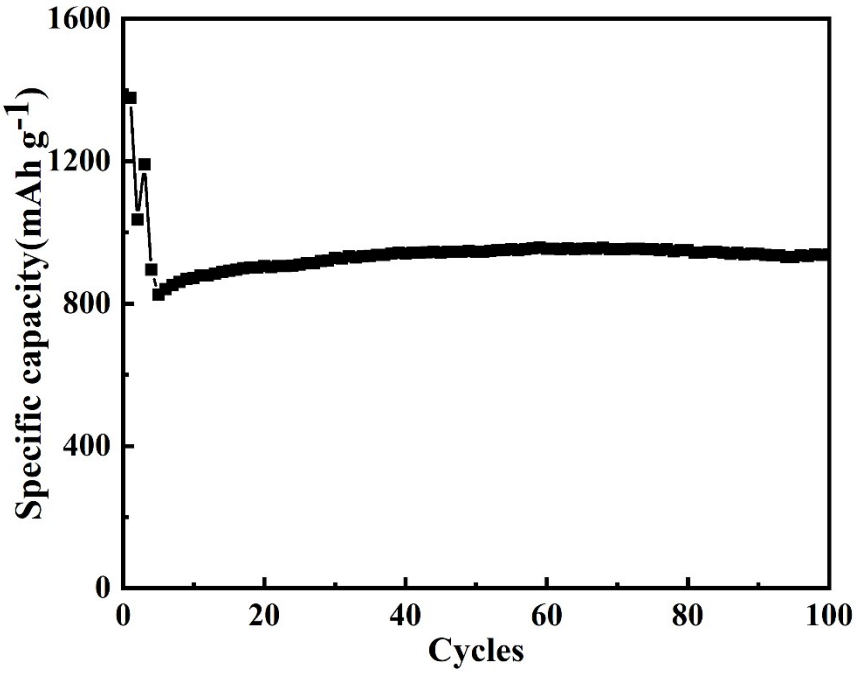

Figure S8 Cycling performance of MMR-SiO_X/C with the mass loading of 2.2 mg cm^{-2}

Figure S8 shows the cycling performance of MMR-SiO_X/C with the high mass loading of 2.2 mg cm^{-2}. Si-based anode with high mass loading is of play in increasing the energy storage capability of lithium-ion batteries for practical application. However, high electrode thickness due to high mass loading is a great challenge to the energy storage capability of LIB. Firstly, thick electrodes over critical cracking thickness lead to mechanical instabilities, even the exfoliation of electrode materials after pressing [1,2]. Secondly, conductivity agents of carbon black, including acetylene black, deliver low, inhomogeneous and unstable electrode conductivity, limiting its electrochemical performance, especially for very thick electrodes [2]. Moreover, the volume fluctuation is more serious during cycling under high mass loading [3]. In our work, the initial specific capacity of MMR-SiO_X/C is as high as 1378.2 mAh g^{-1}, and it retains 937.2 mAh g^{-1} after 100 cycles.

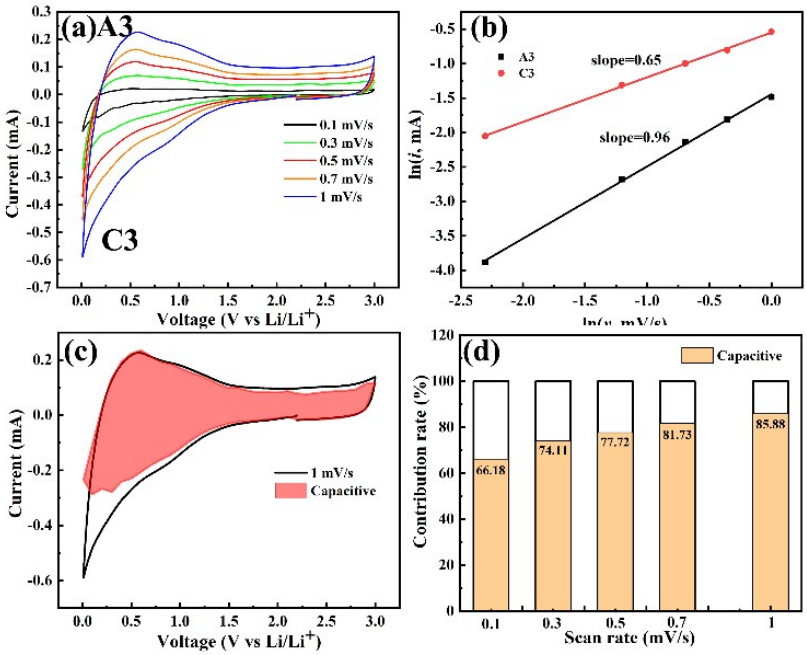

Figure S9 (a) CV curves of HMR-SiO_X/C at different scan rates; (b) fitting lines and ln(peak current) vs ln(scan rate) plots at anode-cathode peaks of HRR-SiO_X/C; (c) the contribution of pseudocapacitance of at HRR-SiO_X/C a scan rate of 1 mV s^{-1}; (d) Capacity contribution at different scan rates of HRR-SiO_X/C.

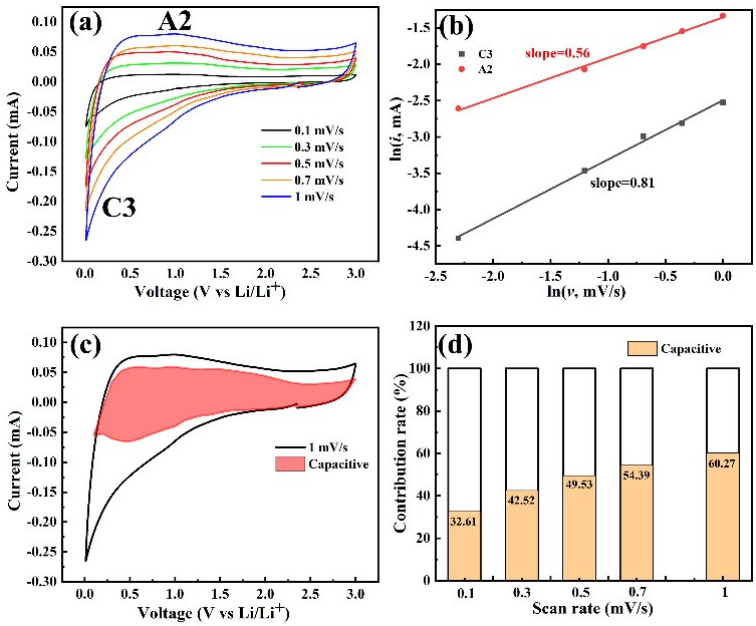

Figure S10 (a) CV curves of LRR-SiO_X/C at different scan rates; (b) fitting lines and ln(peak current) vs ln(scan rate) plots at anode-cathode peaks of LRR-SiO_X/C; (c) the contribution of pseudocapacitance of at LRR-SiO_X/C a scan rate of 1 mV s^{-1}; (d) Capacity contribution at different scan rates of LRR-SiO_X/C.

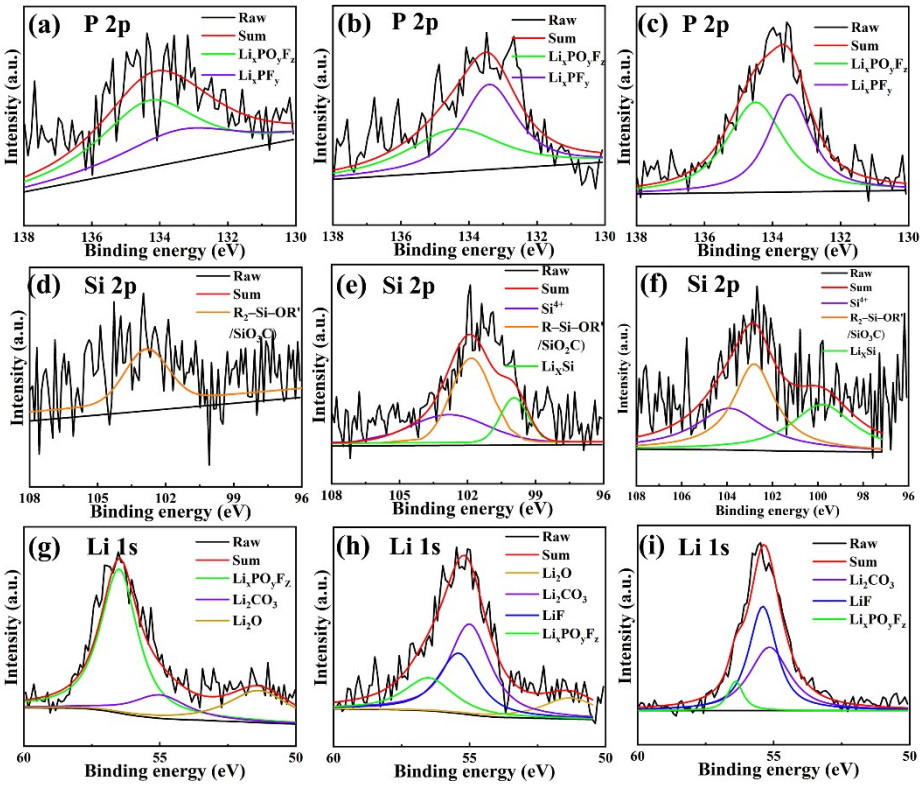

Figure S11 the corresponding high-resolution XPS spectra of HMR-SiO_X/C (a, d, g), MMR-SiO_X/C (b, e, h) and LMR-SiO_X/C (c, f, i) after 100 cycles.

Figures S11 (a)-(c) reveal the existence of $Li_xPO_yF_z$ and Li_xPF_y in three samples, stemming from the decomposition and adsorption of $LiPF_6$. High-resolution Si 2p XPS spectra of HMR-SiO_X/C show the signal of Si^{3+}(103.2eV), ascribed to R_2-Si-OR´ and SiO_3C bonds. Upon cycling, HMR-SiO_X/C suffers from huge volume expansion, leading to the re-exposing of fresh surfaces to the electrolyte. Therefore, it is possible for surficial Si atoms of HMR-SiO_X/C to provide active sites for the continuous decomposition of the electrolyte (increasingly forming SEI layer). Combined with SEM images after cycling (severe pulverization is observed in HMR-SiO_X/C), it is assumed increasingly formed SEI layer majorly contributes to the signal of high-resolution Si 2p XPS spectra of HMR-SiO_X/C. In contrast, the signals of Si^{2+} (102.2eV, R-Si-OR´and SiO_2C) and Si^{3+} in MMR-SiO_X/C and LMR-SiO_X/C are

shown in Figure S11 (e) and (f). Furthermore, Li_xSi signals (99.8 eV) in MMR-SiO_X/C and LMR-SiO_X/C are displayed. These results reveal a thin SEI layer with high stability in MMR-SiO_X/C and LMR-SiO_X/C is formed. On one hand, relatively low volume expansion in MMR-SiO_X/C and LMR-SiO_X/C provides a possibility for a stable SEI layer. On the other hand, a robust adhesion force with the SEI layer further stabilizes the stable interface.

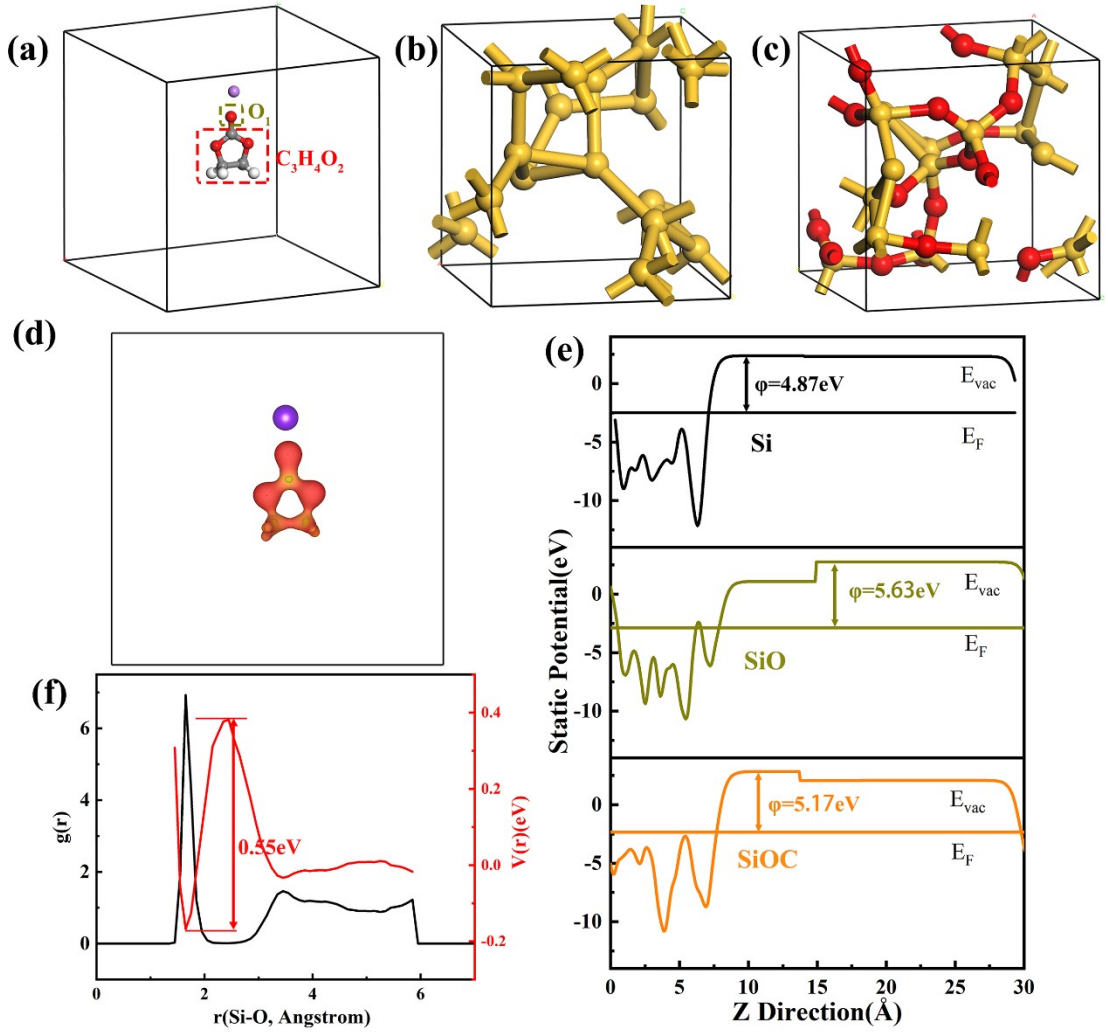

Figure S12 (a) EC:Li^+ model, (b) amorphous Si model, (c) amorphous SiO model, (d) Surface electrostatic potential distribution of EC:Li^+, (e) fitting electrostatic potential, (f) Radial dispersion function $g_{Si-O}(r)$ with estimated mean effective potential energy path for LiSiO (Red:O, Gray:C, White:H, Violet:Li,Yellow:Si)

Ethylene Carbonate (EC) is a typical electrolyte solvent. As the surface electrostatic potential of EC:Li^+ is shown in Figure S12 (d), O_1 species in EC:Li^+ is electron-enriched, posing a robust absorption with Li^+ (electron-depleted) as Figure S12 (a) [4]. EC:Li^+ in the electrolyte tends to be decomposed into free $C_3H_4O_2$ and O_1-Li pairs [5]. Upon cycling, $C_3H_4O_2$ begins to take some electrons for its reduction into organic lithium salts (a typical SEI composition) on the electrode, as well as the

consumption of active lithium. Meanwhile, some inorganic lithium salts, such as LiF, are formed to block the electron transfer into $C_3H_4O_2$ and construct a stable SEI layer. However, SiO_X-based anode suffers from non-negligible volume expansion with local mechanical stress, which induces the delamination of the SEI layer from the electrode, even the pulverization of active anode. Thus, relatively low volume expansion for SiO_X-based anode and a robust adhesion force of EC:Li^+ is of importance in advanced SiO_X-based LIB. As a consequence, some models of absorbing EC:Li^+ are constructed in this work.

As we are known, the electrical conductivity of Si is better than that of SiO_X [6]. Generally, the increase in oxygen content of SiO_X leads to the fading of its electrical conductivity. A typical method is to design and construct SiO_X/C heterostructures for superior electron kinetics. In this work, DFT calculations are used to analyze the electrostatic potential of Si, SiO and SiOC as shown in Figure S12 (e). Further, the work function (φ) of Si, SiO and SiOC is obtained from the equation S1:

$$\varphi = E_{vac} - E_F \qquad \text{(S1)}$$

Here, E_{vac} is the vacuum energy; E_F is fermi energy. Therefore, the φ value of Si, SiO and SiOC, corresponding to Figure S12 (e), is 4.87, 5.63 and 5.17 eV, respectively. It demonstrates the introduction of carbon atoms can boost electrical conductivity.

For the radial dispersion function of Si-O in LiSiO, oxygen atoms are seldom observed between one site (r_{Si-O}=1.65 Å) and another site (r_{Si-O}=3.45 Å), which reveals oxygen cannot diffuse freely. Therefore, in AIMD simulation of LiSiO, Si and O atoms are considered to be relatively still.

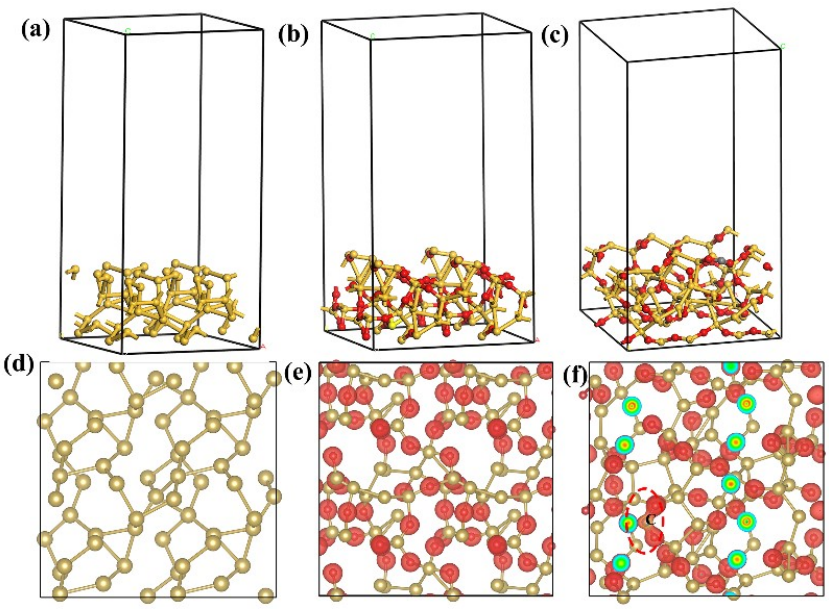

Figure S13 (a) Si model, (b) SiO model and (c) SiOC model, Surface electrostatic potential distribution of (d) Si, (e) SiO and (f) SiOC

Figure S13 shows the Si, SiO and SiOC models with their corresponding Surface electrostatic potential distribution. One finds electron in the Si model is dispersed homogenously, not beneficial to the adsorption of electron-depleted Li^+. In contrast, electrons in SiO and SiOC are almost accumulated in the oxygen region (red region), which partly explains high Li diffusion kinetics in SiO. In addition, the negative electrostatic potential around carbon atoms is lowered, which is due to the reassembly of the electrical field. Therefore, the electron density of the oxygen region around carbon atoms in SiOC is enhanced, extending the electrical field.

Table S1. Elemental Si content with different valence state

	Si	Si^{2+}	Si^{3+}	Si^{4+}	Average valence of Si
HMR-SiO_X/C	2.32%	27.12%	58.28%	12.28%	2.78
MMR-SiO_X/C	0%	15.66%	38.83%	45.51%	3.3
LMR-SiO_X/C	0%	7.72%	47.11%	45.17%	3.4

Table S2. Specific surface area and pore size distribution

	HMR-SiO_X/C	MMR-SiO_X/C	LMR-SiO_X/C
BET Surface area (m^2 g^{-1})	82.01	100.60	105.58
The average pore diameter (nm)	9.85	13.38	10.99

Table S3. Kinetic parameters of HMR-SiO_X/C, MMR-SiO_X/C and LMR-SiO_X/C

		R_S (Ω)	R_{CT} (Ω)	R_{SEI} (Ω)	D_{Li+}(cm^2/s)
HMR-SiO_X/C	Before cycles	5.0	65.1	16.5	/
	100th	6.0	264.2	63.4	$4.12*10^{-18}$
	300th	5.4	278.9	97.8	$6.75*10^{-20}$
MMR-SiO_X/C	Before cycles	9.9	54.0	15.4	/
	100th	5.1	137.5	23.6	$1.68*10^{-18}$
	300th	5.5	107.9	30.9	$1.07*10^{-18}$
LMR-SiO_X/C	Before cycles	7.3	760.0	261.9	/
	100th	7.7	1536.2	332.9	$9.53*10^{-19}$
	300th	8.2	1313.5	470.8	$1.59*10^{-20}$

Table S4 The material parameters in the model

	Young´s modulus (Gpa)	Posson´s ratio	Diffusivity coefficient	Yield stress (Gpa)	Expansion coefficient
Unlithiated Si	160	0.24	0.0005	50	0.002
Fully lithiated Si	40	0.22	0.0005	10	0.002
SiO_2	90	0.17	0.0005	80	0.0001
Carbon	80	0.2	0.0005	25	0

Table S5 supercell volume of Si, SiO, LiSi and LiSiO

	Si	SiO	LiSi	LiSiO
supercell volume(Å^3)	328.51	531.44	504.91	664.93

References

[1] Singh, K.B & Tirumkudulu, M.S., Phys.Rev.Lett. 98 (2007) 218302.

[2] Sang-Hook Park, Paul J. King, et al, Nature Energy 4 (2019) 560-567.

[3] Quan Xu, Jin-Yi Li, et al, Adv. Energy Mater. 7 (2017) 1601481.

[4] L.B. Huang, G. Li, Z.Y. Lu, J.Y. Li, L. Zhao, Y. Zhang, X.D. Zhang, K.C. Jiang, Q. Xu, Y.G. Guo, ACS Appl. Mater. Interfaces 13 (2021) 24916-24924.

[5] J. Rohrer, P. Kaghazchi, Chemphyschem 15 (2014) 3950-3954.

[6] Z. Liu, Q. Yu, Y. Zhao, R. He, M. Xu, S. Feng, S. Li, L. Zhou, L. Mai, Chem. Soc. Rev. 48 (2019) 285-309.